

Photoluminescence Segmentation within Individual Hexagonal Monolayer Tungsten Disulfide Domains Grown by Chemical Vapor Deposition

Yuewen Sheng¹, Xiaochen Wang¹, Kazunori Fujisawa², Siqu Ying³, Ana Laura Elias², Zhong Lin², Wenshuo Xu¹, Yingqiu Zhou¹, Alexander M. Korsunsky³, Harish Bhaskaran¹, Mauricio Terrones^{2,4}, Jamie H. Warner^{1}*

¹Department of Materials, University of Oxford, Parks Road, Oxford OX1 3PH, United Kingdom

²Department of Physics and Center for 2 Dimensional and Layered Materials, The Pennsylvania State University, University Park, PA 16802, USA

³Department of Engineering Science, University of Oxford, Parks Road, Oxford OX1 3PJ, United Kingdom

⁴Department of Chemistry and Department of Materials Science & Engineering, The Pennsylvania State University, University Park, PA 16802, USA

KEYWORDS: 2D materials, tungsten disulfide, monolayer, chemical vapor deposition, photoluminescence

ABSTRACT

We show that hexagonal domains of monolayer WS₂ grown by chemical vapor deposition (CVD) with powder precursors can have discrete segmentation in their photoluminescence

(PL) emission intensity, forming symmetric patterns with alternating bright and dark regions. Two dimensional maps of the PL reveal significant reduction within the segments associated with the longest sides of the hexagonal domains. Analysis of the PL spectra shows differences in the exciton to trion ratio, indicating variations in the exciton recombination dynamics. Monolayers of WS₂ hexagonal islands transferred to new substrates still exhibit this PL segmentation, ruling out local strain regions as the dominant cause. High power laser irradiation causes preferential degradation of the bright segments by sulfur removal, indicating the presence of a more defective region that is higher in oxidative reactivity. Atomic force microscopy (AFM) images of topography and amplitude show uniform thickness of the WS₂ domains and no signs of segmentation. However, AFM phase maps do show the same segmentation of the domain as the PL maps and indicate it is caused by some kind of structural differences that we could not clearly identify. These results provide important insights into the spatially varying properties of these CVD-grown transition metal dichalcogenides (TMDs) materials, which may be important for their effective implementation in fast photo sensors and optical switches.

INTRODUCTION

With the rapid development of two dimensional materials such as metallic graphene¹⁻³ and insulating hexagonal boron nitride,⁴⁻⁷ two-dimensional (2D) transition metal dichalcogenides (TMDs) have recently attracted interest due to their unique semiconducting properties.⁸⁻¹⁵ Monolayer tungsten disulfide (WS₂) and molybdenum disulfide (MoS₂) are TMDs with a direct band gap in the red spectral region that can significantly expand the potential of optoelectronic devices comprising all 2D materials.¹⁶⁻²³

Recently, the properties of monolayer MoS₂ have been studied in mechanically exfoliated, chemically derived, physical vapor deposition grown, and chemical vapor deposition (CVD) grown samples.²⁴⁻²⁸ Their electronic properties can achieve carrier mobilities of $\sim 200 \text{ cm}^2 \text{ V}^{-1} \text{ s}^{-1}$, large excitonic binding energies and can give rise to photoluminescence (PL) spectra that are sensitive to many-body interactions.²⁹⁻³¹ The PL of MoS₂ can be dramatically affected by electrical gating, substitutional doping, and surface functionalization using physical adsorbates or solvents.³²⁻³⁴ It is noteworthy that monolayer WS₂ has a significantly stronger PL signal than single-layer MoS₂, indicative of better prospects for optoelectronic applications.³⁵⁻³⁸

Mechanically exfoliated monolayer WS₂ from synthetic bulk crystals typically has uniform PL across the sample.^{36,37} In addition to the mechanical exfoliation method, many groups around the world have been working on the synthesis of monolayer WS₂ by powder vaporization or chemical vapor transport. Prior work has shown that monolayer WS₂ triangles grown by vaporizing sulfur powders on WO_x thin films, can exhibit non-uniform and uniform PL, respectively.³⁸⁻⁴⁰ In the report of Gutierrez et al.³⁸, the edges of WS₂ monolayers exhibit PL signals with higher intensity, around 25 times stronger than that at the platelet center. The structure and chemical composition of the platelet edges was thought to be critical for PL enhancement.³⁸ Peimyoo et al.³⁹ also found the same phenomenon and claimed that the darkening and the blue-shift of PL are caused by the as-grown structural defects and the defect-induced negative doping. Kim et al.⁴⁰ recently reported that the intense PL emission and the preferential formation of biexcitons at the edges and grain boundaries of monolayer WS₂ were attributed to larger population of charge carriers caused by the excessive incorporation of growth promoters during the CVD. Zhang et al.⁴¹ recently reported a symmetric structure in vapor-deposition fabricated MoS₂ monolayers with symmetrical local bilayer stacking. Raman

spectroscopy indicated that the uniaxial intralayer strain originated from finite boundary and lattice deformation. These results show that uniformity in the PL properties of synthetic grown TMDs varies and needs to be understood further to ensure its role in opto-electronics is adequately described.

Here, we study 2D spatial variations of PL within CVD grown hexagonal monolayer WS₂ crystals grown on silicon substrates with a 300nm oxide layer using powder precursors.^{42,43} Interestingly, the PL emission in the hexagonal domains of WS₂ exhibits segmented variations associated with symmetrically distributed structural variations arising during growth. Optical microscopy, scanning electron microscopy (SEM), atomic force microscopy (AFM), photoluminescence (PL) spectroscopy, Raman spectroscopy, and energy dispersive X-ray spectroscopy (EDX) were all used to characterize the WS₂ monolayers with various shapes in order to elucidate the connection between structure and PL.

RESULTS AND DISCUSSION

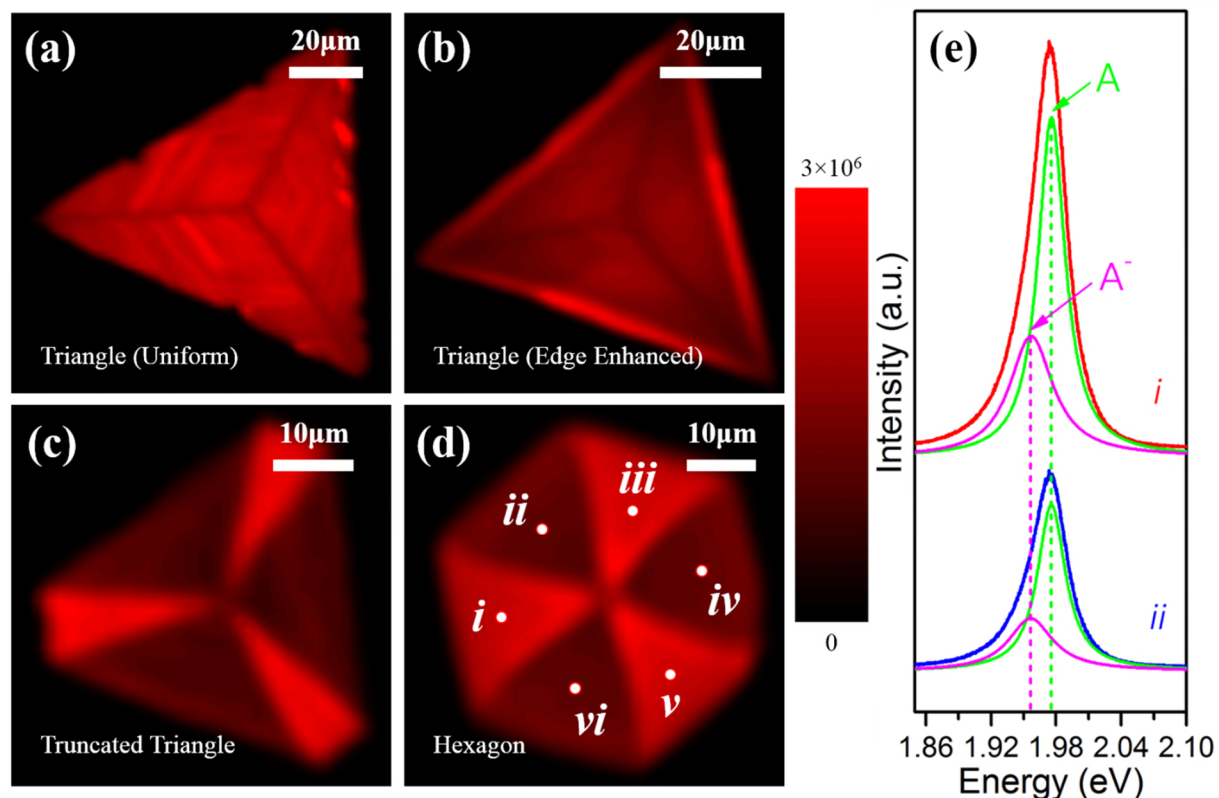


Figure 1. Maps of the integrated PL signals for monolayer WS₂ crystals with different geometric shapes. PL mappings of (a) uniform triangular, (b) edge enhanced triangular, (c) truncated triangular, and (d) hexagonal monolayer WS₂ domains, respectively. Scale bar: 20 μm in (a,b) and 10 μm in (c,d). (e) The corresponding PL spectra of the designated regions in (d). The two representative spectra were fitted by two Lorentzian peaks representing exciton emission (Green) and negative trion emission (Magenta).

Monolayer and bilayer WS₂ can be distinguished by PL and Raman spectroscopy as well as the contrast difference under an optical microscope (see Supporting Information Figure S1). Figure 1 shows the maps of the integrated PL signal for monolayer WS₂ with different geometrical shapes. Prior work on MoS₂ monolayers grown by CVD has shown that shape variation from triangular to hexagon is driven by the relative stoichiometry.^{28,44} Similar shape

evolution has been found in our CVD-grown WS₂ samples, changing from triangles to hexagons along the gas flow direction (see Supporting Information Figure S2). For monolayer WS₂ triangles, two different PL spatial patterns have been previously reported, one with uniform PL distribution and the other with edge-enhanced PL.³⁸⁻⁴⁰ The reduction in PL intensity and its blue-shift in spectral position were associated with as-grown structural defects and defect-induced negatively charged doping.³⁹ Figures 1(a) and (b) show that these two types of triangles are also found in our WS₂ samples. The edges of WS₂ monolayers exhibit PL signals with higher intensity, around 2.5 times stronger than that at the center. According to the previous report, PL enhancement results from the different structure and chemical composition of the platelet edges relative to the centre.³⁸

For non-triangular WS₂ domains, we observe patterns inside the monocrystal, as shown in Figures 1(c) and (d). Due to the low local concentration of sulfur during the growth, some of the WS₂ crystals in the center of the substrate are truncated or hexagonal in shape. Examination by optical microscopy shows they have the same monolayer contrast, indicating that the PL change is not from an increase in layer number (see Supporting Information Figure S3). The two representative PL spectra from the marked spots in a hexagonal monolayer WS₂ domain in Figure 1(d) were compared in Figure 1(e). The PL intensity in the bright areas (marked as i, iii and v in Figure 1(d)) is twice that in the dark areas (designated as ii, iv and vi in Figure 1(d)). The WS₂ PL signal was then deconvoluted into separate peaks by fitting two Lorentzian curves, attributed to exciton emission (A) and negative trion emission (A⁻).^{45,46} The corresponding average photon energies for A and A⁻ in the bright region are 1.976 and 1.957 eV respectively, while the related average photon energies in the dark region are 1.975 and 1.956 eV respectively, showing a difference of ~1 meV in band gap between two regions, which indicates

that the bright areas have slightly more strain introduced during growth than the dark areas.⁴⁷

In addition, the fitting results show differences in the integrated PL intensity ratio of exciton to trion (A/A^-) with an average value of 1.72 for bright area and 1.95 for dark area, indicating a higher level of doping in the bright regions of the hexagonal monolayer of WS_2 (see Supporting Information Table S1).

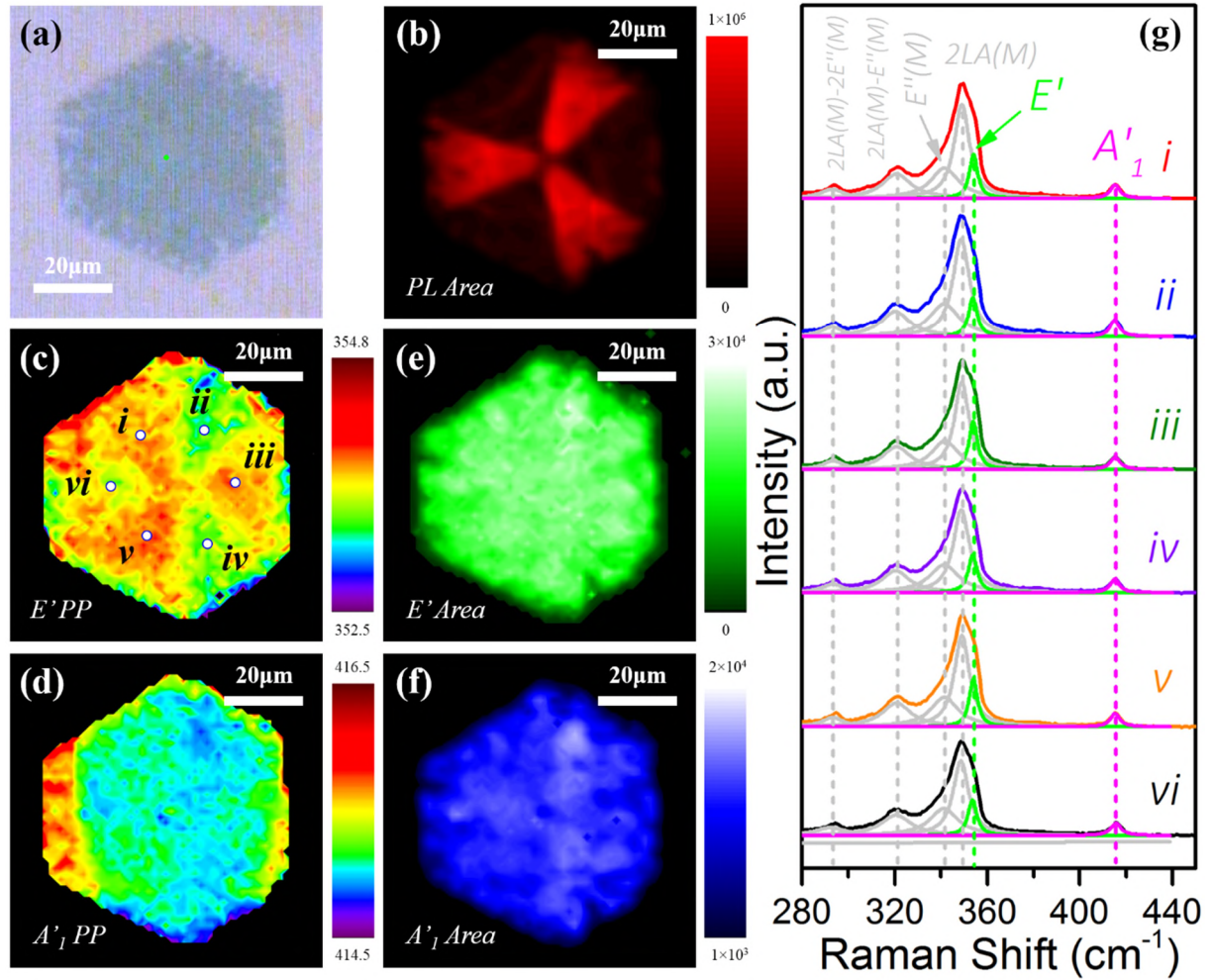


Figure 2. Raman and PL mapping of a hexagonal monolayer WS₂ domain. (a) Optical image of a hexagonal monolayer WS₂ crystal used for Raman mapping. Scale bar: 20 μm. (b-f) PL and Raman mapping obtained from the hexagonal crystal shown in (a), showing (b) PL integrated intensity, (c) E' peak position and (e) integrated intensity as well as (d) A'1 peak position and (f) integrated intensity. Scale bar: 20 μm. (g) The corresponding Raman spectra of the marked regions in (c). All the spectra were fitted by six Lorentzian peaks and two peaks were highlighted, representing E' (Green) and A'1 (Magenta) modes.

In Raman spectroscopy of monolayer WS₂, the E' mode is associated with the in-plane vibration mode for WS₂, while the A'1 mode is associated with an out-of-plane vibration. Figure 2(a) presents the optical image of a typical hexagonal monolayer WS₂ crystal. PL

integrated intensity mapping, Figure 2(b), shows a similar pattern to that seen in Figure 1(d). Figures 2(c-f) show the Raman mapping obtained from the same WS₂ domain, indicating peak position and integrated intensity of the WS₂ E' and A'₁ modes. As can be seen from the Raman mappings, a small blue-shift of $\sim 0.3 \text{ cm}^{-1}$ for the peak position of E' mode was found from the PL bright areas compared with the PL dark regions and very small variations were found in both A'₁ integrated intensity and peak position mapping. These mappings are totally different from those Raman mappings taken from monolayer WS₂ with symmetric multilayer stacking, which show an obvious distinction between monolayer and few-layer WS₂ (see Supporting Information Figure S4). Again, we took six Raman spectra from the marked spots in hexagonal monolayer WS₂, Figure 2(c), for further discussion. As shown in Figure 2(g), no obvious difference can be observed from the overall spectra. Using a Lorentzian fitting, Raman signals ranging from 280 to 440 cm^{-1} can be deconvolved into six separate peaks, two of which can be attributed to WS₂ E' and A'₁ vibration modes.³⁵ The corresponding peak positions for the A'₁ mode are about 415.2 cm^{-1} on average for both bright and dark regions, confirming that there is no observable distinction in A'₁ peak positions, corresponding to the effect of inhomogeneous external electrostatic doping, between PL of the bright and dark regions. In addition, the corresponding E' mode peak position is 354.0 cm^{-1} on average for the area with lower PL intensity (marked as i, iii and v in Figure 2(c)) and 353.7 cm^{-1} for that with higher PL intensity (designated as ii, iv and vi in Figure 2(c)) (see Supporting Information Table S2).

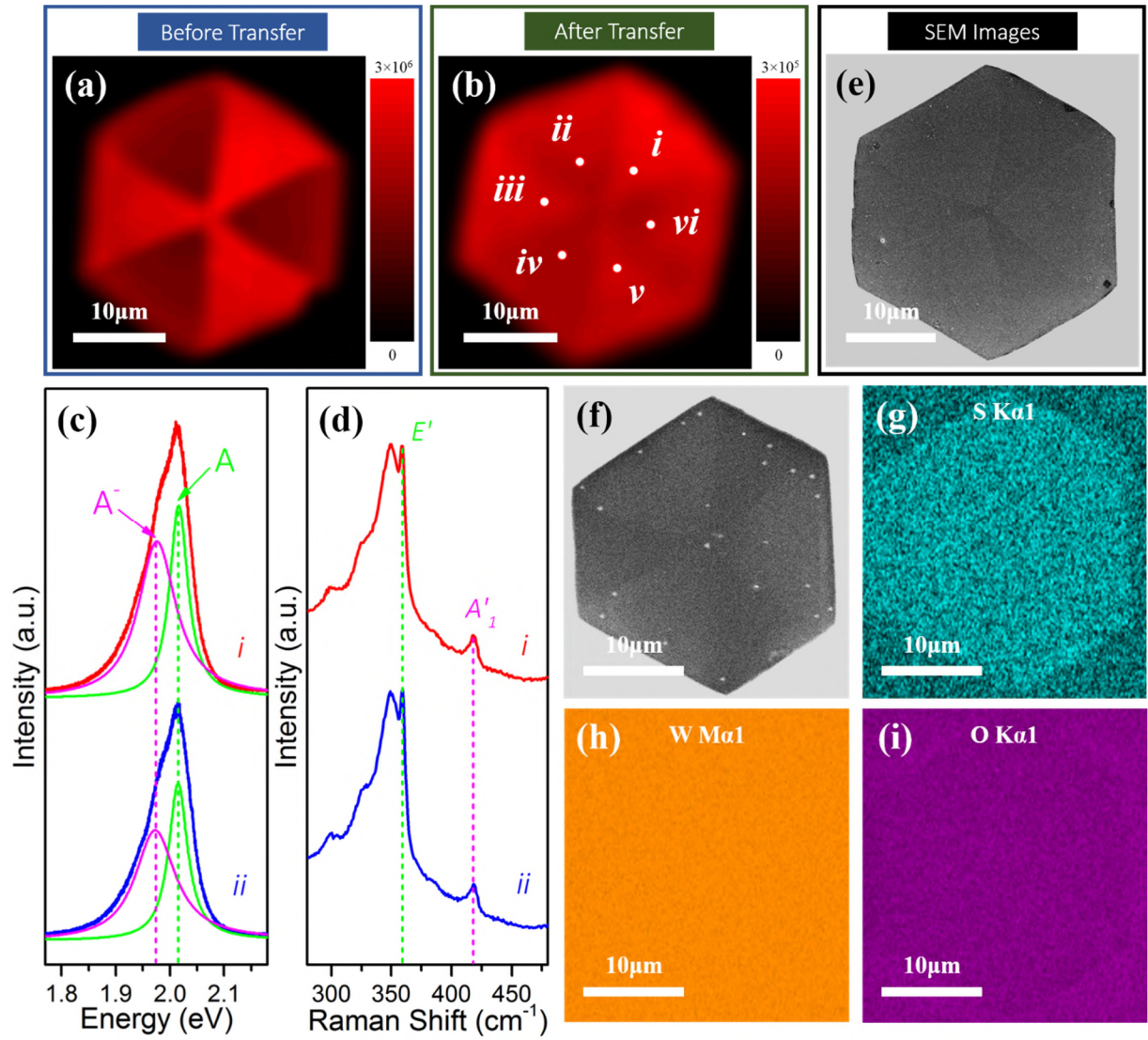


Figure 3. Characterization of hexagonal monolayer WS₂ before and after transfer. (a,b) Typical PL integrated mapping of (a) as-grown and (b) transferred WS₂ domains on SiO₂/Si. Scale bar: 10 μm. (c,d) The corresponding (c) PL and (d) Raman spectra of the marked regions in (b). The two representative PL spectra were fitted by two Lorentzian peaks representing exciton emission (Green) and negative trion emission (Magenta). (e) SEM image of a typical as-grown hexagonal WS₂ crystal on SiO₂/Si, showing similar symmetric pattern. Scale bar: 10 μm. (f-i) EDX elemental mappings of a pristine hexagonal monolayer WS₂ domain shown in (f), indicating the distribution of (g) Sulfur, (h) Tungsten and (i) Oxygen, respectively. Scale bar: 10 μm.

To investigate if strain is the dominant mechanism in the symmetric PL segmentation, we mapped the PL of the sample before and after transferring to another SiO₂/Si chip. Strain from the rapid cooling during growth is known to be released when transferred to a new substrate. No baking process was involved during the transfer process in order to prevent strain being generated due to the different thermal expansion coefficients of WS₂ and the substrate. Figure 3(a) presents the PL integrated mapping of a typical as-grown hexagonal monolayer WS₂ domain. The PL intensity ratio of bright to dark area differs from sample to sample, ranging from 2-3. After transferring the WS₂ from growth substrate to another SiO₂/Si substrate, we observed an overall reduction of PL intensity both from the bright region and the dark region. The larger reduction of PL intensity occurred for the bright area, decreasing by a factor of ~10.5, while the reduction was only by a factor of ~6.5 for the dark region. Although the release of strain during the transfer process would introduce impurities to the sample and degrade the quantum yield of the direct transition within monolayer WS₂, we can still observe the PL patterns from mapping results with a PL intensity ratio of ~1.2, Figure 4(b). Figure 3(d) depicts the two representative Raman spectra taken from the designated points in Figure 3(b). The peak positions of E' and A'₁ modes for both regions are the same, with values of 358.3 and 418.0 cm⁻¹, respectively. The PL spectra from six marked spots in Figure 3(b) were also plotted for further comparison. Figure 3(c) shows the two representative PL spectra, fitted with two Lorentzian peaks, correlating to A and A⁻ respectively. The corresponding average peak positions for A and A⁻ in the bright area (noted as i, iii and v in Figure 3(b)) are 2.015 and 1.974 eV respectively, same as the peak positions in the dark area (noted as ii, iv and vi in Figure 3(b)). The variation between two regions in peak positions for both Raman and PL spectra is negligible, confirming that strain has been successfully released. However, the strain-free hexagonal sample still shows difference in A/A⁻ ratio (see Supporting Information Table S3).

The ratio in the bright area is smaller than that in the dark area, the trend of which is similar to the as-grown sample. It implies that strain might not be the dominant factor causing the symmetric PL pattern. Figure 3(e) shows the high-resolution SEM image of a typical hexagonal WS₂ domain. It is not as obvious as in the as-grown sample, but similar pattern can be observed which implies that it might be caused by structural imperfections or physical adsorbates. The EDX results, Figures 3(g-i), show no measureable spatial patterns for a typical as-grown hexagonal monolayer WS₂ domain, the SEM image of which can be seen in Figure 3(f). This might be due to the ultrathin nature of the material, making it difficult to detect subtle variations using EDX.

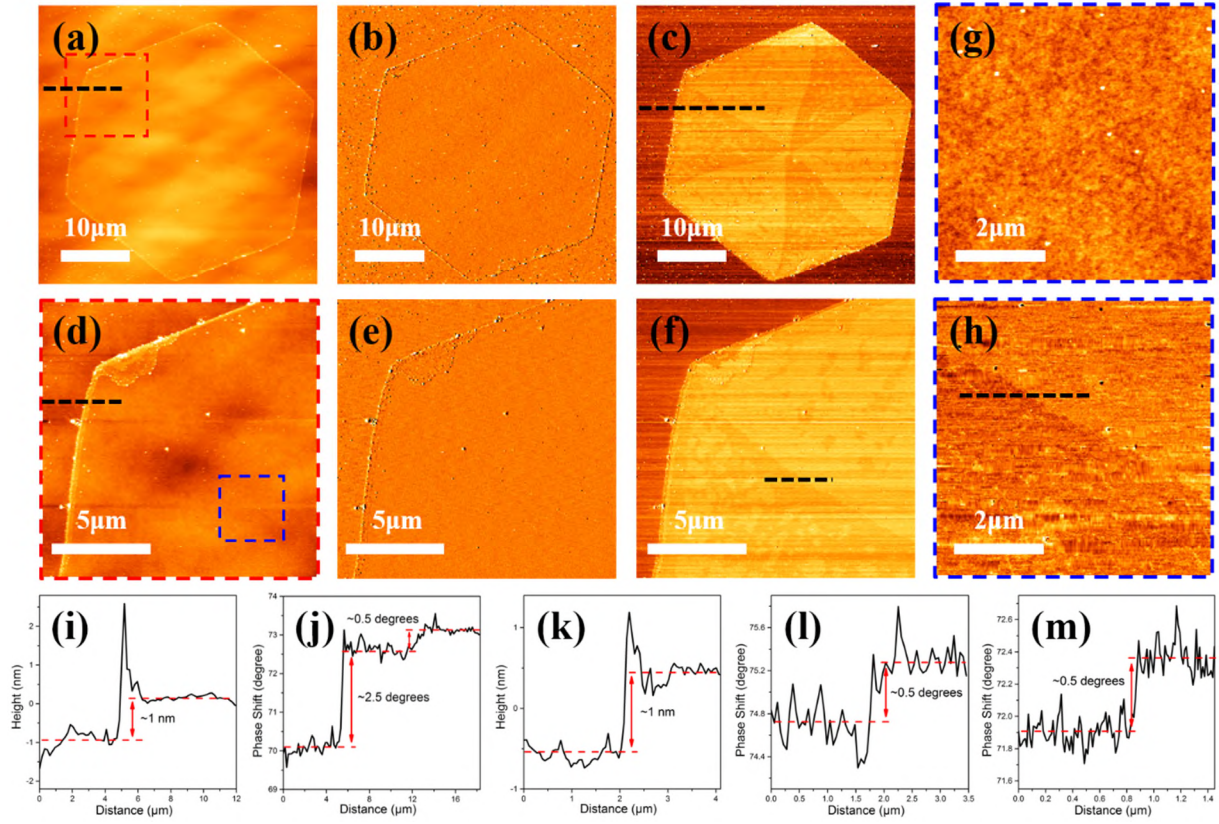


Figure 4. Atomic Force Microscopy measurements of a monolayer hexagonal WS₂ crystal. (a-c) AFM images of (a) topography, (b) amplitude and (c) phase modes, respectively, for a typical monolayer hexagonal WS₂ crystal. Scale bars: 10 μm. (d-f) Zoomed-in AFM maps of the red dashed square in (a), showing (d) height, (e) amplitude and (f) phase modes, respectively. Scale bar: 5 μm. (g,h) Further zoomed-in images of the blue dashed region in (d), presenting (g) topology and (h) phase modes, respectively. Scale bar: 2 μm. (i-m) The (i) height and (j) phase profiles taken from the black dashed line in (a) and (c). The (k) height and (l) phase profiles taken across the black dashed line in (d) and (f). (m) The corresponding phase profile taken from black dashed line in (h).

AFM was then used to probe changes in the WS₂ domains across the regions of differing PL by assessing the maps produced from topography, amplitude and phase measurements, Figure 4. As can be seen from the surface morphology shown in Figures 4(a, d, g), the topography is quite uniform and no similar pattern is found in the crystal, which is in agreement with our

optical microscope images (see Supporting Information Figure S3). From Figures 4(i) and (k), the height difference between the crystal and the substrate is measured to be around 1nm, indicative of monolayer WS₂. Figure 4(g) is the further magnified image of the blue dashed square in Figure 4(d), indicating no topography difference at the edge of two areas with different PL intensities. AFM images in amplitude mode, Figures 4(b) and (e), showed a uniform distribution pattern. Therefore, variation in surface adsorbates can be ruled out for the non-uniform PL pattern because they would be detected as a variation in the height maps. The phase mode map is shown in Figure 4(c) with differences between the WS₂ and SiO₂ seen and associated with elasticity changes of the two materials. The phase profile in Figure 4(j) shows that the phase change of the AFM tip vibration is $\sim 2.5^\circ$ when moving from the surface of SiO₂ to monolayer WS₂. Within the WS₂ domain, a spatial pattern in the phase map is seen, Figure 4(c), with a phase change of $\sim 0.5^\circ$ between the two areas, and this correlates to the same pattern observed in the maps of the PL intensities, Figure 4(d). The phase profiles in Figures 4(j, l, m) indicate that the regions with different PL intensities may have variations in surface stiffness/softness and adhesion between the tip and surface, which can be attributed to the slight difference in structure between the two areas.

The characterization results shown in Figures 1-4 reveal that neither physical adsorbates nor doping from the dielectric environment contribute to the observed difference in PL intensity mapping. The 2D monolayer WS₂ crystal is anisotropic and the laser used for PL and Raman spectroscopy is polarized, but no change was found when rotating the stage during measurements, indicating the symmetric pattern is not related to the polarized incident light (see Supporting Information Figure S5). The relative spatial variations in strain within the WS₂ upon cooling after growth may impact the distribution of defects in the material, and defects in

a 2D semiconductor can trap free charge carriers and localize excitons, which leads to a change in the intrinsic PL.⁴⁸⁻⁵⁰

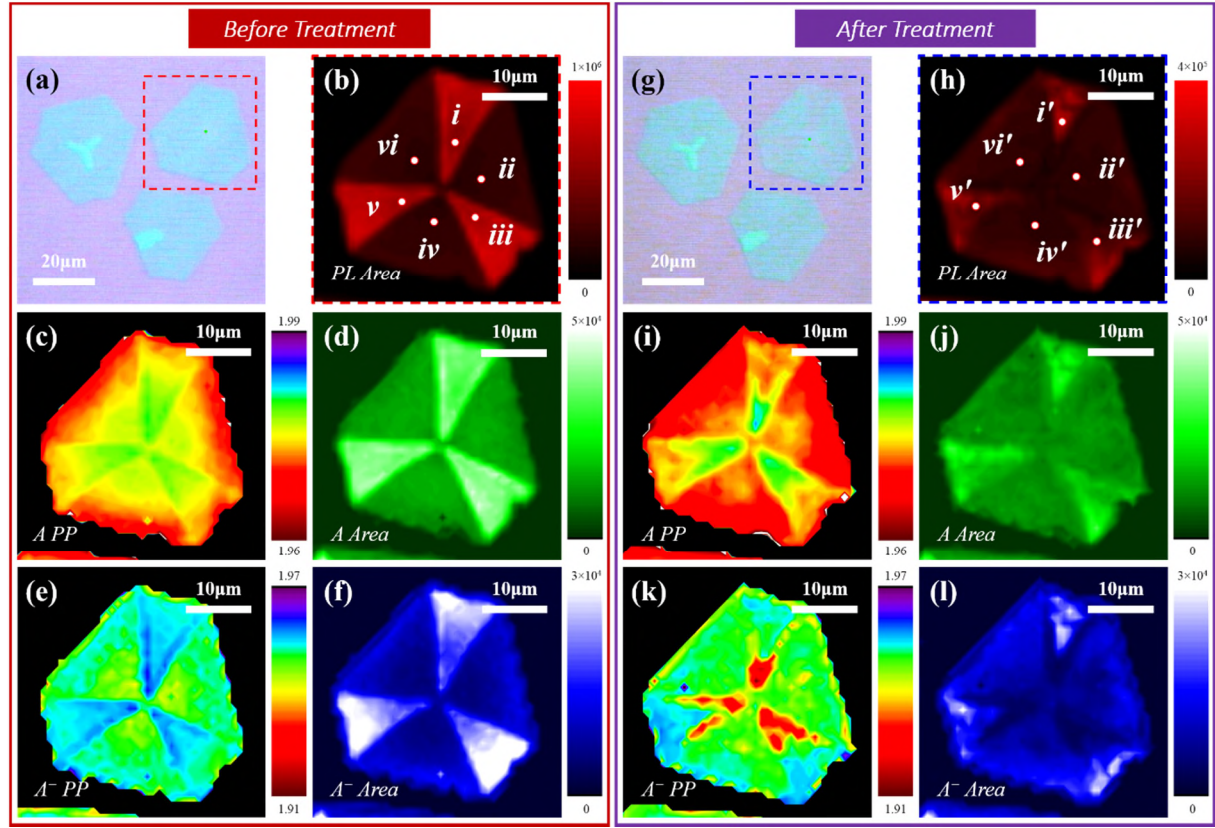


Figure 5. Characterization of as-grown WS₂ domain before and after degradation. (a) Optical image of WS₂ domains before high power laser exposure. The red dashed square indicates the region for PL mapping. Scale bar: 20 μm . (b) PL integrated intensity mapping of the corresponding WS₂ crystal before treatment. Scale bar: 10 μm . (c-f) PL mappings of the same WS₂ crystal, showing spatial distributions of (c) A peak position, (d) A integrated intensity, (e) A⁻ peak position and (f) A⁻ integrated intensity respectively. Scale bar: 10 μm . (g) Optical images of WS₂ domains after high power laser exposure. Scale bar: 20 μm . (h) PL mapping of the corresponding WS₂ crystal highlighted with blue dashed square in (g). Scale bar: 10 μm . (i-l) PL mappings of the same WS₂ crystal after treatment, showing spatial distributions of (i) A peak position, (j) A integrated intensity, (k) A⁻ peak position and (l) A⁻ integrated intensity respectively. Scale bar: 10 μm .

Defective regions of WS₂ should be more sensitive to oxidation and to probe this we exposed the sample to a higher power laser to accelerating oxidative decomposition of the sample.

Figure 5(a) shows the optical image of three WS₂ domains, the contrast difference indicates different thickness of the WS₂ grown by powder vaporization. Figure 5(b) presents the PL integrated intensity mapping of the region highlighted with red dashed line in Figure 5(a). Figures 5(c-f) present the PL fitting results of the same crystal, showing obvious variation in the mappings of A peak position, A integrated intensity, A⁻ peak position and A⁻ integrated intensity. We took six spots from each side of the pristine hexagonal monolayer WS₂ (Figure 5(b)) for further discussion. It was found that, before treatment, the dark areas (designated as ii, iv and vi in Figure 5(b)) had only about one-third of PL intensity obtained from the bright areas (marked as i, iii and v in Figure 5(b)). After Lorentzian curve fitting, the average peak positions for A and A⁻ are 1.977 and 1.958 eV in bright region and 1.976 and 1.951 eV in dark region respectively. The fitting results (see Supporting Information Table S4) show difference in A/A⁻ ratio with an average value of 1.94 for bright areas and 2.89 for dark areas, the trend of which is consistent with our previous untreated PL data. After higher-power laser exposure, the area with higher PL integrated intensity degrades, leaving similar pattern as what PL mapping previously showed, Figure 5(g). As can be seen from Figure 5(h), the intensity of the degraded area was significantly quenched, even lower than the dark areas on the untreated sample (noted as ii, iv and vi in Figure 5(b)). Figures 5(i-l) show the corresponding PL maps of the treated sample. The difference can be clearly seen compared with the untreated PL maps, Figures 5(c-f). The corresponding peak positions for A and A⁻ of the dark regions (designated as ii', iv' and vi' in Figure 5(h)) redshifted to 1.969 and 1.950 eV respectively. The similar phenomenon can also be found in the bright areas (noted as i', iii' and v' in Figure 5(h)), with A and A⁻ peaks red-shifting to 1.973 and 1.956 eV respectively.

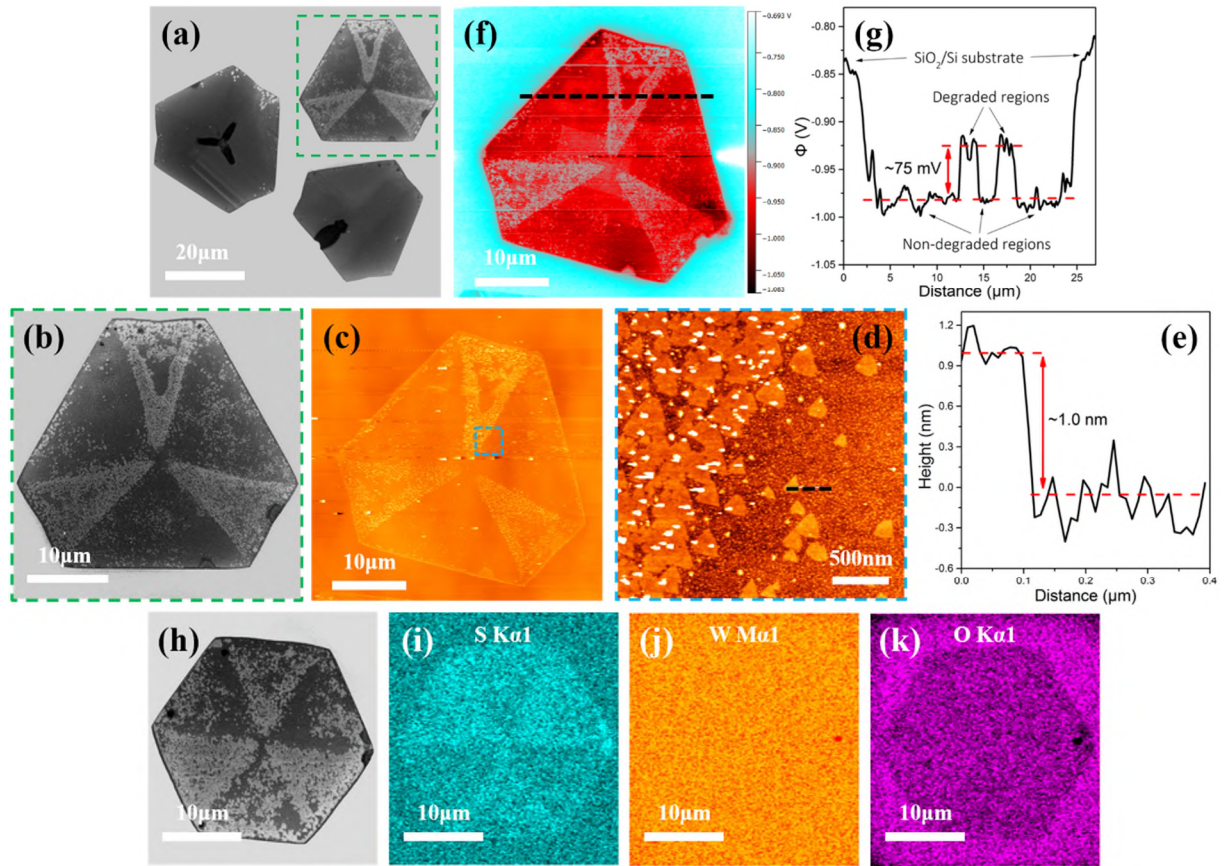


Figure 6. Characterization of the preferentially degraded WS₂ after high-power laser exposure.

(a) SEM image of the degraded WS₂ on SiO₂/Si. Scale bar: 20 μm. (b) Zoomed-in SEM image of the green dashed area in (a). Scale bar: 10 μm. (c) AFM topological mapping of the green dashed highlighted region in (a). Scale bar: 10 μm. (d) Zoomed-in AFM image of the selected area marked in cyan dashed square in (c). Scale bar: 500 nm. (e) Corresponding height profile taken across the black dashed line in (d), showing the height difference between degraded and non-degraded areas is about 1 nm. (f,g) AFM image in KPM mode and the corresponding profile taken from the black dashed line in (f), showing the work function difference between two areas is about 75 mV. Scale bar: 10 μm. (h) SEM image of a degraded hexagonal WS₂ on SiO₂/Si. Scale bar: 10 μm. (i-k) EDX elemental mapping of the same crystal in (h), indicating the distribution of (i) Sulfur, (j) Tungsten and (k) Oxygen respectively. Scale bar: 10 μm.

Figure 6(a) shows the SEM image of the same area as in Figure 5, but after high power laser exposure. The contrast difference between monolayer and multilayer WS₂ seen from the optical image, Figure 5(a), can also be observed under SEM. Figure 6(b) is the magnified SEM image of the green dashed region in Figure 6(a). Figures 6(c) and (f) show the AFM surface morphology and Kelvin Probe Microscopy (KPM) images of the degraded WS₂ crystal respectively. As can be seen from Figure 6(d), the degraded area was formed of small triangles, which is in agreement with SEM images (see Supporting Information Figure S6). The height difference between the brighter triangle and the monolayer WS₂ is about 1 nm, Figure 6(e). In addition, as shown in Figure 6(g), the work function increased by 75 mV after degradation, and the work function of the degraded areas is closer to the SiO₂/Si substrate compared with that of non-degraded areas, indicating that the degraded part might be oxidized into an insulating material. Figures 6(g-k) present the EDX elemental mapping (S, W, O) of a degraded hexagonal WS₂ crystal shown in Figure 6(h), respectively. As can be seen from Figures 6(i) and (k), the degraded area corresponds to the region with less Sulfur and more Oxygen elements, confirming that the oxidation has taken place during degradation.

CONCLUSION

In summary, we showed that the discrete symmetric segmented PL patterns from hexagonal monolayer WS₂ are associated with structural variations, and not surface adsorbates or secondary layers of WS₂. Only slight changes in peak positions from PL and Raman spectra are observed, suggesting that the strain introduced during the growth might be a minor factor and that doping from the dielectric environment due to different adhesion to the substrate can be discounted. In addition, AFM images in topology mode show no height difference between the two areas with different PL intensity, which can help us rule out physical adsorbates. A

difference in A/A^- ratio for both the as-grown sample and strain-free sample was found, implying that the structural imperfections may play a major role in PL spatial distribution. The segmentation of defects might be caused during the CVD cooling process and these findings can give insight into the PL properties of hexagonal monolayer WS_2 , which could expand the application of this semiconducting material in the future.

EXPERIMENTAL METHODS

Synthesis of CVD Monolayer WS_2

The CVD monolayer WS_2 domains were grown using our previously reported CVD approach^{42,43} using Sulfur and WO_3 as powder based precursors. Sulfur and WO_3 were placed in a 1 inch quartz tube running through a double-furnace system to provide two heating zones. Vaporized Sulfur and WO_3 were carried by a flow of argon gas to the reaction zone, where WO_3 undergoes sulfurization. High quality and large size hexagonal monolayer WS_2 crystals were fabricated on SiO_2/Si when growth conditions including temperature, argon flow rate and growth time were optimized.

Transfer of CVD Monolayer WS_2

The as-grown CVD hexagonal WS_2 domains were transferred onto other arbitrary substrates using the non-aqueous sliding transfer method.²³ The samples were first spin-coated with a PMMA scaffold (8 wt% in anisole, 495k molecular weight) at 4500 rpm for 1 min and then cured at 180°C for 90 seconds. The SiO_2/Si substrate was detached from WS_2 by floating the sample on a 1M Potassium hydroxide (KOH) (90%, Sigma–Aldrich) solution in a water bath at 45°C. The floating film was then transferred to DI water in beakers three times with at least 30min per rinse. The subsequent steps involve (i) dipping a piece of clean cover glass into DI

water, (ii) pushing it towards the floating film, (iii) scooping the film onto the cover glass, (iv) wetting the cover glass with some IPA, (v) pipetting some IPA onto the target substrate, which is kept horizontal on the desk, followed by (vi) resting one side of the cover glass on the edge of the target substrate and (vii) lifting the other side up slightly, allowing the film to slide down very slowly. Finally, after being left dry in a fume hood overnight, the transferred sample was then placed in acetone for 2-3 hours to remove PMMA.

Characterization of as-grown and treated WS₂ samples

The structural characteristics of the WS₂ crystals on SiO₂/Si were observed using a scanning electron microscope (Hitachi-4300) with an accelerating voltage of 3.0 kV. The SEM-EDX analysis was conducted using a TESCAN LYRA Multi-beam system equipped with an EDX detector (Oxford Instruments). EDX data were acquired at 5 keV for 6-8 hours in order to get a clear contrast difference within the hexagonal domains. Raman and photoluminescence (PL) spectroscopies were carried out using a JY Horiba LabRAM Aramis imaging confocal Raman microscope with an excitation wavelength of 532 nm with an estimated laser spot size of 1 μm. The laser power was 12.5 mW and 125 μW for Raman and PL respectively. Topological characterizations of as-grown and treated WS₂ were performed using an atomic force microscope (Asylum Research MFP-3D) in AC mode with a silicon AC-160TS cantilever (Olympus, spring constant ~42 N/m and resonant frequency ~300 kHz). Measurements were all done in room-temperature under ambient pressure.

ACCOCIATED CONTENT

Supporting Information

The Supporting Information is available free of charge via the Internet at <http://pubs.acs.org>. Additional experiment results including identification of monolayer and bilayer WS₂, optical images of monolayer WS₂ in different shapes, characterization of monolayer WS₂ with symmetric multilayer stacking, PL mappings of hexagonal WS₂ at different rotation angles, optical and SEM images of degraded WS₂ crystal as well as the fitting results of the PL and Raman spectra (PDF)

Corresponding Author

*Email: jamie.warner@materials.ox.ac.uk.

Notes

The authors declare no competing financial interest.

ACKNOWLEDGEMENTS

J.H.W. thanks the Royal Society for support. Y.S. acknowledges support from the Armourers & Brasiers Gauntlet Trust.

REFERENCES

- (1) Geim, A. K.; Novoselov, K. S. The Rise of Graphene. *Nat. Mater.* **2007**, *6*, 183–191.
- (2) Novoselov, K. S. Nobel Lecture: Graphene: Materials in the Flatland. *Rev. Mod. Phys.* **2011**, *83*, 837–849.
- (3) Sheng, Y.; Rong, Y.; He, Z.; Fan, Y.; Warner, J. H. Uniformity of Large-Area Bilayer Graphene Grown by Chemical Vapor Deposition. *Nanotechnology* **2015**, *26*, 395601.

- (4) Gao, T.; Song, X.; Du, H.; Nie, Y.; Chen, Y.; Ji, Q.; Sun, J.; Yang, Y.; Zhang, Y.; Liu, Z. Temperature-Triggered Chemical Switching Growth of In-plane and Vertically Stacked Graphene-Boron Nitride Heterostructures. *Nat. Commun.* **2015**, *6*, 6835.
- (5) Dean, C. R.; Young, A. F.; Meric, I.; Lee, C.; Wang, L.; Sorgenfrei, S.; Watanabe, K.; Taniguchi, T.; Kim, P.; Shepard, K. L.; Hone J. Boron Nitride Substrates for High-Quality Graphene Electronics. *Nat. Nanotechnol.* **2010**, *5*, 722–726.
- (6) Ci, L.; Song, L.; Jin, C.; Jariwala, D.; Wu, D.; Li, Y.; Srivastava, A.; Wang, Z. F.; Storr, K.; Balicas, L.; Liu, F.; Ajayan, P. M. Atomic Layers of Hybridized Boron Nitride and Graphene Domains. *Nat. Mater.* **2010**, *9*, 430–435.
- (7) Kim, K. K.; Hsu, A.; Jia, X.; Kim, S. M.; Shi, Y.; Hofmann, M.; Nezich, D.; Rodriguez-Nieva, J. F.; Dresselhaus, M.; Palacios, T.; Kong, J. Synthesis of Monolayer Hexagonal Boron Nitride on Cu Foil Using Chemical Vapor Deposition. *Nano Lett.* **2012**, *12*, 161–166.
- (8) Fang, H.; Chuang, S.; Chang, T. C.; Takei, K.; Takahashi, T.; Javey, A. High-Performance Single Layered WSe₂ P-FETs with Chemically Doped Contacts. *Nano Lett.* **2012**, *12*, 3788–3792.
- (9) Lebègue, S.; Eriksson, O. Electronic Structure of Two-Dimensional Crystals from Ab Initio Theory. *Phys. Rev. B* **2009**, *79*, 115409.
- (10) Li, T.; Galli, G. Electronic Properties of MoS₂ Nanoparticles. *J. Phys. Chem. C* **2007**, *111*, 16192–16196.

- (11) Cheiwchanchamnangij, T.; Lambrecht, W. R. L. Quasiparticle Band Structure Calculation of Monolayer, Bilayer, and Bulk MoS₂. *Phys. Rev. B* **2012**, *85*, 1–4.
- (12) Wang, H.; Yu, L.; Lee, Y.; Shi, Y.; Hsu, A.; Chin, M. L.; Li, L.; Dubey, M.; Kong, J.; Palacios, T. Integrated Circuits Based on Bilayer MoS₂ transistors. *Nano Lett.* **2012**, *12*, 4674–4680.
- (13) Zeng, H.; Dai, J.; Yao, W.; Xiao, D.; Cui, X. Valley Polarization in MoS₂ Monolayers by Optical Pumping. *Nat. Nanotechnol.* **2012**, *7*, 490–493.
- (14) Jones, A. M.; Yu, H.; Ghimire, N. J.; Wu, S.; Aivazian, G.; Ross, J. S.; Zhao, B.; Yan, J.; Mandrus, D. G.; Xiao, D.; Yao, W.; Xu, X. Optical Generation of Excitonic Valley Coherence in Monolayer WSe₂. *Nat. Nanotechnol.* **2013**, *8*, 634–638.
- (15) He, Z.; Sheng, Y.; Rong, Y.; Lee, G.; Li, J.; Warner, J. H. Layer-Dependent Modulation of Tungsten Disulfide Photoluminescence by Lateral Electric Fields. *ACS Nano* **2015**, *9*, 2740–2748.
- (16) Sundaram, R. S.; Engel, M.; Lombardo, A.; Krupke, R.; Ferrari, A. C.; Avouris, P.; Steiner, M. Electroluminescence in Single Layer MoS₂. *Nano Lett.* **2013**, *13*, 1416–1421.
- (17) Rong, Y.; Sheng, Y.; Pacios, M.; Wang, X.; He, Z.; Bhaskaran, H.; Warner, J. H. Electroluminescence Dynamics across Grain Boundary Regions of Monolayer Tungsten Disulfide. *ACS Nano* **2016**, *10*, 1093–1100.
- (18) Tsai, M. L.; Su, S. H.; Chang, J. K.; Tsai, D. S.; Chen, C. H.; Wu, C. I.; Li, L. J.; Chen, L. J.; He, J. H. Monolayer MoS₂ Heterojunction Solar Cells. *ACS Nano* **2014**, *8*, 8317–8322.

- (19) Lopez-Sanchez, O.; Lembke, D.; Kayci, M.; Radenovic, A.; Kis, A. Ultrasensitive Photodetectors Based on Monolayer MoS₂. *Nat. Nanotechnol.* **2013**, *8*, 497–501.
- (20) Yang, W.; Shang, J.; Wang, J.; Shen, X.; Cao, B.; Peimyoo, N.; Zou, C.; Chen, Y.; Wang, Y.; Cong, C.; Huang, W.; Yu, T. Electrically Tunable Valley-Light Emitting Diode (vLED) Based on CVD-Grown Monolayer WS₂. *Nano Lett.* **2016**, *16*, 1560–1567.
- (21) Cheng, R.; Li, D.; Zhou, H.; Wang, C.; Yin, A.; Jiang, S.; Liu, Y.; Chen, Y.; Huang, Y.; Duan, X. Electroluminescence and Photocurrent Generation from Atomically Sharp WSe₂/MoS₂ Heterojunction P-N Diodes. *Nano Lett.* **2014**, *14*, 5590–5597.
- (22) Withers, F.; Del Pozo-Zamudio, O.; Mishchenko, A.; Rooney, A. P.; Gholinia, A.; Watanabe, K.; Taniguchi, T.; Haigh, S. J.; Geim, A. K.; Tartakovskii, A. I.; Novoselov, K. S. Light-Emitting Diodes by Band-Structure Engineering in van Der Waals Heterostructures. *Nat. Mater.* **2015**, *14*, 301–306.
- (23) Sheng, Y.; Xu, W.; Wang, X.; He, Z.; Rong, Y.; Warner, J. H. Mixed Multilayered Vertical Heterostructures Utilizing Strained Monolayer WS₂. *Nanoscale* **2016**, *8*, 2639–2947.
- (24) Splendiani, A.; Sun, L.; Zhang, Y.; Li, T.; Kim, J.; Chim, C. Y.; Galli, G.; Wang, F. Emerging Photoluminescence in Monolayer MoS₂. *Nano Lett.* **2010**, *10*, 1271–1275.
- (25) Coleman, J. N.; Lotya, M.; O'Neill, A.; Bergin, S. D.; King, P. J.; Khan, U.; Young, K.; Gaucher, A.; De, S.; Smith, R. J.; Shvets, I. V.; Arora, S. K.; Stanton, G.; Kim, H.-Y.; Lee, K.; Kim, G. T.; Duesberg, G. S.; Hallam, T.; Boland, J. J.; Wang, J. J.; Donegan, J. F.; Grunlan, J. C.; Moriarty, G.; Shmeliov, A.; Nicholls, R. J.; Perkins, J. M.; Grievson, E. M.; Theuwissen, K.; McComb, D. W.; Nellist, P. D.; Nicolosi, C. Two-Dimensional

- Nanosheets Produced by Liquid Exfoliation of Layered Materials. *Science* **2011**, *331*, 568–571.
- (26) Lauritsen, J. V.; Kibsgaard, J.; Topsøe, H.; Helveg, S.; Clausen, B. S.; Laegsgaard, E.; Besenbacher, F. Size-Dependent Structure of MoS₂ Nanocrystals. *Nat. Nanotechnol.* **2007**, *2*, 53–58.
- (27) van der Zande, A. M.; Huang, P. Y.; Chenet, D. A.; Berkelbach, T. C.; You, Y.; Lee, G.-H.; Heinz, T. F.; Reichman, D. R.; Muller, D. A.; Hone, J. C. Grains and Grain Boundaries in Highly Crystalline Monolayer Molybdenum Disulphide. *Nat. Mater.* **2013**, *12*, 554–561.
- (28) Wang, S.; Rong, Y.; Fan, Y.; Pacios, M.; Bhaskaran, H.; He, K.; Warner, J. H. Shape Evolution of Monolayer MoS₂ Crystals Grown by Chemical Vapor Deposition. *Chem. Mater.* **2014**, *26*, 6371–6379.
- (29) Radisavljevic, B.; Radenovic, A.; Brivio, J.; Giacometti, V.; Kis, A. Single-Layer MoS₂ Transistors. *Nat. Nanotechnol.* **2011**, *6*, 147–150.
- (30) Yin, Z.; Li, H.; Li, H.; Jiang, L.; Shi, Y.; Sun, Y.; Lu, G.; Zhang, Q.; Chen, X.; Zhang, H. Single-Layer MoS₂ Phototransistors. *ACS Nano* **2012**, *6*, 74–80.
- (31) Lee, S.; Lee, K.; Zhong, Z. Wafer Scale Homogeneous Bilayer Graphene Films by Chemical Vapor Deposition. *Nano Lett.* **2010**, *10*, 4702–4707.
- (32) Mak, K. F.; He, K.; Lee, C.; Lee, G. H.; Hone, J.; Heinz, T. F.; Shan, J. Tightly Bound Trions in Monolayer MoS₂. *Nat. Mater.* **2013**, *12*, 207–211.

- (33) Tongay, S.; Zhou, J.; Ataca, C.; Liu, J.; Kang, J. S.; Matthews, T. S.; You, L.; Li, J.; Grossman, J. C.; Wu, J. Broad-Range Modulation of Light Emission in Two-Dimensional Semiconductors by Molecular Physisorption Gating. *Nano Lett.* **2013**, *13*, 2831–2836.
- (34) Lee, Y. H.; Yu, L.; Wang, H.; Fang, W.; Ling, X.; Shi, Y.; Lin, C. Te; Huang, J. K.; Chang, M. T.; Chang, C. S.; Dresselhaus, M.; Palacios, T.; Li, L. J.; Kong, J. Synthesis and Transfer of Single-Layer Transition Metal Disulfides on Diverse Surfaces. *Nano Lett.* **2013**, *13*, 1852–1857.
- (35) Berkdemir, A.; Gutiérrez, H. R.; Botello-Méndez, A. R.; Perea-López, N.; Elías, A. L.; Chia, C.-I.; Wang, B.; Crespi, V. H.; López-Urías, F.; Charlier, J.-C.; Terrones, H.; Terrones, M. Identification of Individual and Few Layers of WS₂ Using Raman Spectroscopy. *Sci. Rep.* **2013**, *3*, 1–8.
- (36) Zhao, W.; Ghorannevis, Z.; Chu, L.; Toh, M.; Kloc, C.; Tan, P.-H.; Eda, G. Evolution of Electronic Structure in Atomically Thin Sheets of WS₂ and WSe₂. *ACS Nano* **2013**, *7*, 791–797.
- (37) Zeng, H.; Liu, G.-B.; Dai, J.; Yan, Y.; Zhu, B.; He, R.; Xie, L.; Xu, S.; Chen, X.; Yao, W.; Cui, X. Optical Signature of Symmetry Variations and Spin-Valley Coupling in Atomically Thin Tungsten Dichalcogenides. *Sci. Rep.* **2013**, *3*, 1608.
- (38) Gutiérrez, H. R.; Perea-López, N.; Laura, A.; Berkdemir, A.; Wang, B.; Terrones, M. Extraordinary Room-Temperature Photoluminescence in Triangular WS₂ Monolayers. *Nano Lett.* **2013**, *13*, 3447–3454.

- (39) Peimyoo, N.; Shang, J.; Cong, C.; Shen, X.; Wu, X.; Yeow, E. K. L.; Yu, T. Nonblinking, Intense Two-Dimensional Light Emitter: Monolayer WS₂ Triangles. *ACS Nano* **2013**, *7*, 10985–10994.
- (40) Kim, M. S.; Yun, S. J.; Lee, Y.; Seo, C.; Han, G. H.; Kim, K. K.; Lee, Y. H.; Kim, J. Biexciton Emission from Edges and Grain Boundaries of Triangular WS₂ Monolayers. *ACS Nano* **2016**, *10*, 2399–2405.
- (41) Zhang, K.; Hu, S.; Zhang, Y.; Zhang, T.; Zhou, X.; Sun, Y.; Li, T.-X.; Fan, H. J.; Shen, G.; Chen, X. Self-Induced Uniaxial Strain in MoS₂ Monolayers with Local van Der Waals-Stacked Interlayer Interactions. *ACS Nano* **2015**, *9*, 2704–2710.
- (42) Rong, Y.; He, K.; Pacios, M.; Robertson, A. W.; Bhaskaran, H.; Warner, J. H. Controlled Preferential Oxidation of Grain Boundaries in Monolayer Tungsten Disulfide for Direct Optical Imaging. *ACS Nano* **2015**, *9*, 3695–3703.
- (43) Rong, Y.; Fan, Y.; Leen Koh, A.; Robertson, A. W.; He, K.; Wang, S.; Tan, H.; Sinclair, R.; Warner, J. H. Controlling Sulphur Precursor Addition for Large Single Crystal Domains of WS₂. *Nanoscale* **2014**, *6*, 12096–12103.
- (44) Govind Rajan, A.; Warner, J. H.; Blankschtein, D.; Strano, M. S. Generalized Mechanistic Model for the Chemical Vapor Deposition of 2D Transition Metal Dichalcogenide Monolayers. *ACS Nano* **2016**, *10*, 4330–4344.
- (45) Shang, J.; Shen, X.; Cong, C.; Peimyoo, N.; Cao, B.; Eginligil, M.; Yu, T. Observation of Excitonic Fine Structure in a 2D Transition Metal Dichalcogenide Semiconductor. *ACS Nano* **2015**, *9*, 647–655.

- (46) Ross, J. S.; Wu, S.; Yu, H.; Ghimire, N. J.; Jones, A. M.; Aivazian, G.; Yan, J.; Mandrus, D. G.; Xiao, D.; Yao, W.; Xu, X. Electrical Control of Neutral and Charged Excitons in a Monolayer Semiconductor. *Nat. Commun.* **2013**, *4*, 1474.
- (47) Conley, H. J.; Wang, B.; Ziegler, J. I.; Haglund, R. F.; Pantelides, S. T.; Bolotin, K. I. Bandgap Engineering of Strained Monolayer and Bilayer MoS₂. *Nano Lett.* **2013**, *13*, 3626–3630.
- (48) Nan, H.; Wang, Z.; Wang, W.; Liang, Z.; Lu, Y.; Chen, Q.; He, D.; Tan, P.; Miao, F.; Wang, X.; Wang, J.; Ni, Z. Strong Photoluminescence Enhancement of MoS₂ through Defect Engineering and Oxygen Bonding. *ACS Nano* **2014**, *8*, 5738–5745.
- (49) Tongay, S.; Suh, J.; Ataca, C.; Fan, W.; Luce, A.; Kang, J. S.; Liu, J.; Ko, C.; Raghunathanan, R.; Zhou, J.; Ogletree, F.; Li, J.; Grossman, J. C.; Wu, J. Defects Activated Photoluminescence in Two-Dimensional Semiconductors: Interplay between Bound, Charged, and Free Excitons. *Sci. Rep.* **2013**, *3*, 2657.
- (50) Su, W.; Jin, L.; Qu, X.; Huo, D.; Yang, L. Defect Passivation Induced Strong Photoluminescence Enhancement of Rhombic Monolayer MoS₂. *Phys. Chem. Chem. Phys.* **2016**, *18*, 14001–14006.

TOC GRAPHICS

